NANO-PATTERNING OF SURFACES BY ION SPUTTERING: NUMERICAL STUDY OF THE KURAMOTO-SIVASHINSKY EQUATION BY IMPLICIT TIME SPLITTING *

Eduardo Vitral[1]
Daniel Walgraef[2]
José Pontes[3]
Gustavo Rabello dos Anjos[4]
Norberto Mangiavacchi[5]

Abstract
The present study focuses in the simulation of pattern formation by ion beam sputtering on a material surface. This process is responsible for the appearance of unexpectedly organized patterns, such as ripples, nanodots and hexagonal arrays of nanoholes. A numerical analysis of preexisting patterns is proposed to investigate surface dynamics, based on a model derived from a Kuramoto-Sivashinsky anisotropic equation, in a two dimensional surface with periodic boundary conditions. While deterministic, its highly nonlinear character gives a rich range of results, making it possible to describe accurately different patterns. A finite-difference semi-implicit splitting scheme is employed on the discretization of the governing equation. Simulations were conducted with realistic coefficients related to physical parameters (anisotropies, beam orientation, diffusion). The study dealt with a random and a monomode 1D structure initial condition in order to understand how the shape and wavelength of the initial pattern evolve with time. Ripples and hexagonal patterns were observed in the results, being physically consistent with the phenomenon. Moreover, the Method of Manufactured Solution has been used as verification of the developed numerical scheme.
Keywords: Kuramoto-Sivashinsky equation; Sputtering; Finite-difference method.

1 *Materials Engineer, Graduate student, GESAR, UERJ, Rio de Janeiro, Brazil.*
2 *DSc , Associated staff, IFISC, University of Balearic Islands, Palma de Mallorca, Spain.*
3 *DSc, Senior researcher, GESAR, UERJ, Rio de Janeiro, Brazil.*
4 *PhD, Professor, GESAR, UERJ, Rio de Janeiro, Brazil.*
5 *PhD, Professor, GESAR, UERJ, Rio de Janeiro, Brazil.*

* *Technical contribution to the 70º Congresso Anual da ABM – Internacional and to the 15º ENEMET - Encontro Nacional de Estudantes de Engenharia Metalúrgica, de Materiais e de Minas, part of the ABM Week, August 17th-21st, 2015, Rio de Janeiro, RJ, Brazil.*

1 INTRODUCTION

During the last decades, huge advances in materials science technologies permitted the processing of new materials and structures through the operation in nonequilibrium conditions, dodging the limitations imposed by equilibrium thermodynamics. Among the techniques, some of the best known are: ion implantation, spark plasma sintering, laser beam melting, glow discharge sputtering and ion beam sputtering. The theoretical comprehension of such processes is still an ongoing challenge and their mathematical modeling needs more development. Our effort aims toward the development of a numerical scheme to solve a model proposed to the ion beam sputtering erosion.

The phenomenon consists on the ionic bombardment of a surface, spontaneously developing a well-ordered periodicity over a large area under certain conditions [1]. This physical process responsible for the formation of periodic structures on the previously surface is called sputtering. Depending on the energy of the incident ion, a train of collision event may be established, resulting in the ejection of atoms from the matrix. The morphology of the surface can drastically change due to these sputtered atoms, being responsible for the appearance of unexpectedly organized patterns, such as ripples, nanodots and hexagonal arrays of nanoholes (see [2], [3] and [4]). Valbusa et al. [5] discussed the interplay between ion erosion and vacancies on the surface re-organization, which would explain some of the patterns experimentally detected. The rate of energy deposition is a crucial parameter for the mechanisms, since high values can lead to a local transient melting of the surface [3], alongside the possibility of ion implantation.

Continuum theories have been studied to describe surfaces eroded by ion bombardment, reproducing ripple formation and other organized patterns. The Kuramoto-Sivashinsky equation, which was initially formulated to describe flame fronts and chemical waves [6], is deterministic and highly nonlinear, being capable of producing a great variety of morphologies. Rost et al. [7] describes the equation as being remarkable for the stabilization of the linear instability by the nonlinear term. This stabilization makes the equation a good candidate to represent the complexity behind the structure formation on sputtered surfaces, with a dynamic transiting between different regimes.

In the present endeavor, a finite-difference semi-implicit splitting scheme of second order in time and space is proposed to numerically solve an anisotropic Kuramoto-Sivashinsky equation subjected to periodical boundary conditions for two dimensional surfaces. Internal iterations are used inside each time step to enhance the approximation of the nonlinear term. Previously, a similar numerical scheme was successfully implemented for the Swift-Hohenberg Equation by Chistov et al. [8,9], which also dealt with the challenges of high-order spatial derivatives and nonlinearity. The numerical scheme is verified by the Method of Manufactured Solutions, and the simulation results are discussed in the light of the experimental evidences and linear stability analysis predictions. Hexagonal patterns were obtained from a random initial condition, while a 1D structure constructed with a function sine in the $\vec{1}_x$ direction split its wavelength in two transiting to the steady state, without losing its unidimensional quality.

2 MATERIAL AND METHODS

2.1 Governing Equations

The present study proposes a second order in time finite difference numerical scheme for solving modifications of the generalized Kuramoto-Sivashinsky equation [5,6,10-12]. For the case of isotropic energy distribution, considering an ion beam with angle of incidence θ with respect to the normal of the surface, one dimensionless and simplified form of the equation reads:

$$\frac{\partial \bar{h}}{\partial \tau} = -\alpha\bar{h} + \mu\frac{\partial^2\bar{h}}{\partial X^2} - c^2\frac{\partial^2\bar{h}}{\partial Y^2} + \nu_x\left(\frac{\partial\bar{h}}{\partial X}\right)^2 - c^3\left(\frac{\partial\bar{h}}{\partial Y}\right)^2 - D_{xx}\frac{\partial^4\bar{h}}{\partial X^4} + D_{xy}\frac{\partial^4\bar{h}}{\partial X^2\partial Y^2} + c^2\frac{\partial^4\bar{h}}{\partial Y^4} - K\left(\frac{\partial^4\bar{h}}{\partial^4 X} + 2\frac{\partial^4\bar{h}}{\partial X^2\partial Y^2} + \frac{\partial^4\bar{h}}{\partial Y^4}\right) \quad (1)$$

where $\bar{h}$ and τ are, respectively, the surface height function of the external atom layer and the time dependency of the transient model, with X and Y as the domain space coordinates. The function *c* represents the cosine of the incident angle θ. Equation 1 presents a damping term -$\alpha\bar{h}$, with α being a damping coefficient, contributing to the smoothening of the surface [13]. Finally, K takes into account the surface diffusion effects, which varies with temperature. The parameters μ, ν_x, D_{xx} and D_{xy} will be defined as follows:

$$\mu = 2s^2 - c^2 - a_\mu^2 s^2 c^2 \qquad D_{xx} = \left[c^2 - 4s^2 + 2a_\mu^2 s^2\left(c^2 - \frac{2}{3}s^2\right) + \frac{a_\mu^4}{3}s^4c^2\right]$$

$$\nu_x = c\left(3s^2 - c^2 - a_\mu^2 s^2 c^2\right) \qquad D_{xy} = 2\left(3c^2 - 2s^2 + a_\mu^2 s^2 c^2\right)$$

Here, *s* is the sine of θ and $\boldsymbol{a_\mu}$ is the ratio between the ionic penetration depth and the width of energy distribution. In order to solve Equation 1, the following second order in time Cranck-Nicholson semi-implicit scheme [6,7] was adopted:

$$\frac{\bar{h}^{n+1} - \bar{h}^n}{\Delta\tau} = \Lambda_X^{n+1/2}\left(\bar{h}^{n+1} + \bar{h}^n\right) + \Lambda_Y^{n+1/2}\left(\bar{h}^{n+1} + \bar{h}^n\right) + f^{n+1/2} \quad (2)$$

The superscript (*n*+1) refers to the *current* time and (*n*) to the *previous* one. The operators $\Lambda_X^{n+1/2}$, $\Lambda_Y^{n+1/2}$ and the function $f^{n+1/2}$ are defined as:

$$\Lambda_X^{n+1/2} = \frac{1}{2}\left[-\frac{\alpha}{2} - (D_{XX} + K)\frac{\partial^4}{\partial X^4}\right] \quad (3)$$

$$\Lambda_Y^{n+1/2} = \frac{1}{2}\left[-\frac{\alpha}{2} - K\frac{\partial^4}{\partial Y^4}\right] \quad (4)$$

$$f^{n+1/2} = \frac{1}{2}\left[\mu\frac{\partial^2}{\partial X^2} - c^2\frac{\partial^2}{\partial Y^2} + \nu_x\left(\frac{\partial\bar{h}^{n+1}}{\partial X} + \frac{\partial\bar{h}^n}{\partial X}\right)\frac{\partial}{\partial X} - c^3\left(\frac{\partial\bar{h}^{n+1}}{\partial Y} + \frac{\partial\bar{h}^n}{\partial Y}\right)\frac{\partial}{\partial Y} + (D_{XY} - 2K)\frac{\partial^4}{\partial X^2\partial Y^2} + c^2\frac{\partial^4}{\partial Y^4}\right]\left(\bar{h}^{n+1} + \bar{h}^n\right) \quad (5)$$

2.2 Internal Iterations

Internal iterations at each time step are required to secure the approximation for the nonlinearities taking part in the scheme of Equation 2. The iterations loop will continue until convergence is attained from monitoring the L_∞ norm. There is a trade-off related to the time step $\Delta\tau$: for a larger $\Delta\tau$, convergence will be impaired and the number of internal iterations will increase, while a smaller $\Delta\tau$ will impact on a smaller number of iterations, but it will imply on a greater number of time steps. The internal iterations scheme reads:

$$\frac{\bar{h}^{n,m+1} - \bar{h}^{n}}{\Delta\tau} = \Lambda_X^{n+1/2}\left(\bar{h}^{n,m+1} + \bar{h}^{n}\right) + \Lambda_Y^{n+1/2}\left(\bar{h}^{n,m+1} + \bar{h}^{n}\right) + f^{n+1/2} \quad (6)$$

where the index *m* refers to the internal iteration number. The superscript (*n*,*m* + 1) identifies the *new* iteration, while (*n*) are the values of the previous time step. The superscript (*n*+1) for the nonlinear term in the function $\boldsymbol{f^{n+1/2}}$ will be replaced by (*n*,*m*), which stands for the values obtained from the previous iteration. The iterations proceed until the following criterion for the $\boldsymbol{L_\infty}$ norm is satisfied:

$$L_\infty = \frac{max\left|\bar{h}^{n,m+1} - \bar{h}^{n,m}\right|}{max\left|\bar{h}^{n,m+1}\right|} < 10^{-6} \quad (7)$$

for all points of the grid for a fixed *m*. The function $\bar{h}^{n+1}$ for the current time will be acquired from $\bar{h}^{n,m+1}$, proceeding to the last iteration.

2.3 The Splitting Scheme

The splitting of Equation 2 is made according to the second Douglas scheme [14,15]. Such strategy has been chosen to deal with the costly procedure of solving Equation 5; even though we are working with sparse matrices for the operators, the internal iterations cause the process to be repeated several times during each time step. This problem welcomes an attempt to minimize the operations per unit iteration, as follows:

$$\frac{\tilde{\bar{h}} - \bar{h}^{n}}{\Delta\tau} = \Lambda_X^{n+1/2}\tilde{\bar{h}} + \Lambda_Y^{n+1/2}\bar{h}^{n} + f^{n+1/2} + (\Lambda_X^{n+1/2} + \Lambda_Y^{n+1/2})\bar{h}^{n} \quad (8)$$

$$\frac{\bar{h}^{n,m+1} - \tilde{\bar{h}}}{\Delta\tau} = \Lambda_Y^{n+1/2}(\bar{h}^{n,m+1} - \bar{h}^{n}) \quad (9)$$

Here, $\tilde{\bar{h}}$ is the height function for the *half-time* step. Not only can it be shown that the splitting represents the original scheme, but it is also more stable than the original.

2.4 The Method of Manufactured Solution (MMS)

The MMS is a code verification procedure, which analyses if a computational model and its implementation code stand for the task of representing the mathematical model of a physical event with sufficient accuracy. The idea behind the MMS is to solve a problem as if the analytical solution was available from start, creating a manufactured solution for a system of partial differential equations [16]. Considering

that the proposed function is unlikely to solve the equations exactly, a residual term will appear due to the solution of the linear system. By inserting such term in the right-hand side of the equation as a source term, a different numerical solution may be obtained, which is expected to approach the artificial analytical solution (if the manufactured equation was properly constructed). The global discretization error can be examined by the L_2 norm:

$$L_2 = \left(\frac{\sum_{i=1}^{N} \left| \bar{h}_{i,k}^{n} - \bar{h}_{i,m}^{n} \right|}{N} \right)^{1/2} \quad (10)$$

where N is the total number of mesh nodes, $\boldsymbol{i}$ is the index of each node, and the index k and m design the numerical and the manufactured solution, respectively. Such norm analyses how the numerical solution approaches its corresponding analytical solution after each time step. It is indeed expected that the error will decrease by refining the mesh.

3 RESULTS AND DISCUSSION

3.1 Validation and Verification

In consonance with the guidelines for the manufactured solution construction from Roache [17], an artificial solution $\bar{h}_m$ was developed for the height function, which is sensible to spatio-temporal variations:

$$\bar{h}_m = h_o + h_{xy} \sin\left(\frac{a_x \pi x}{L}\right) \cos\left(\frac{a_y \pi x}{L}\right) e^{b\tau} \quad (11)$$

The parameter values employed in the manufactured solution and in the differential equation are presented in Table 1. The artificial terms h_o , h_{xy} , a_x , a_y and b were chosen arbitrarily. Although there is no need for the artificial solution to be realistic, the chosen values were coherent with the main simulations. All tests took place in a quadratic domain, with side $L = 256$, and fixed time step $\Delta\tau = 0.1$.

Table 1. Parameter values for the manufactured solution.

MS Parameters	Value	KS Parameters	Value
h_o	0	K	5
h_{xy}	10^{-4}	a_μ	4
a_x	2	θ	30°
a_y	2	α	0.15
b	-1/200	$\Delta\tau$	0.1

Figure 1 shows how the spatial grid refinement affects the global discretization error, plotting the L_2 norm for five different grid spacing g_s. The error trends toward second-order convergence with respect to grid spacing for coarser meshes, while it stands between first and second-order convergence for more refined meshes. The manufactured solution was unstable for the analyzed differential equation, which grows rapidly in time until its saturation, dominating the result over the source term. For such reason, we limited the range of analysis to a stable region for the artificial function, where the numerical solution converges with the analytical solution.

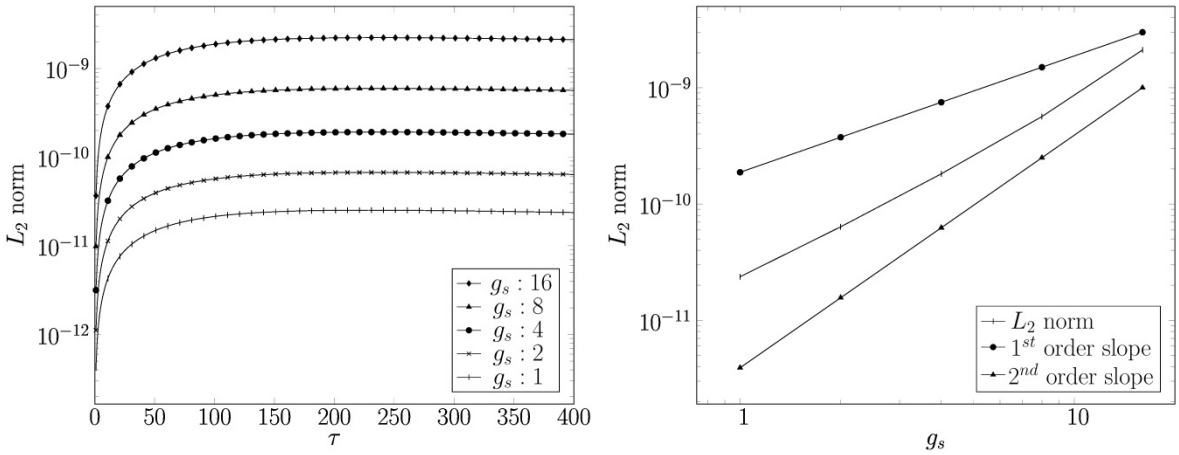

Figure 1. Evolution in time of the L2 norm for the manufactured comparing different grid spacing (left panel). First and second order error lines are also displayed for comparison (right panel).

3.2 Initial Pattern: Random Values

The first case analyzed was for a mesh with 256×256 points with a randomly generated initial pattern, ranging from 0 to 0.1, and parameters α, θ, K and a_μ as found in Table 1. Since the side of the domain is $L_x = L_y = 512$, and the linear stability analysis reveals a value of $\lambda_c = 18$ for the critical wavelength corresponding to the maximum growth rate in the $\vec{1}_x$ direction, each wavelength of the final pattern was expected to be represented by approximately 9 points.

We monitored the rate of evolution of the pattern during the simulation by the L_1 norm, which indicates how fast the structure is changing between the current and previous time step, normalized by the spatial average of the modulus of the surface height. This norm is denoted as:

$$L_1 = \frac{\sum_{ij} \left| \bar{h}_{ij}^{n+1} - \bar{h}_{ij}^{n} \right|}{\Delta\tau \sum_{ij} \left| \bar{h}_{ij}^{n+1} \right|} \quad (12)$$

The pattern evolution was monitored until $L_1 < 1 \times 10^{-6}$, when we assume that the steady state was reached. Figure 2 presents the L_1 norm decay for the random initial pattern, alongside the maximum height modulus value for a certain time step.

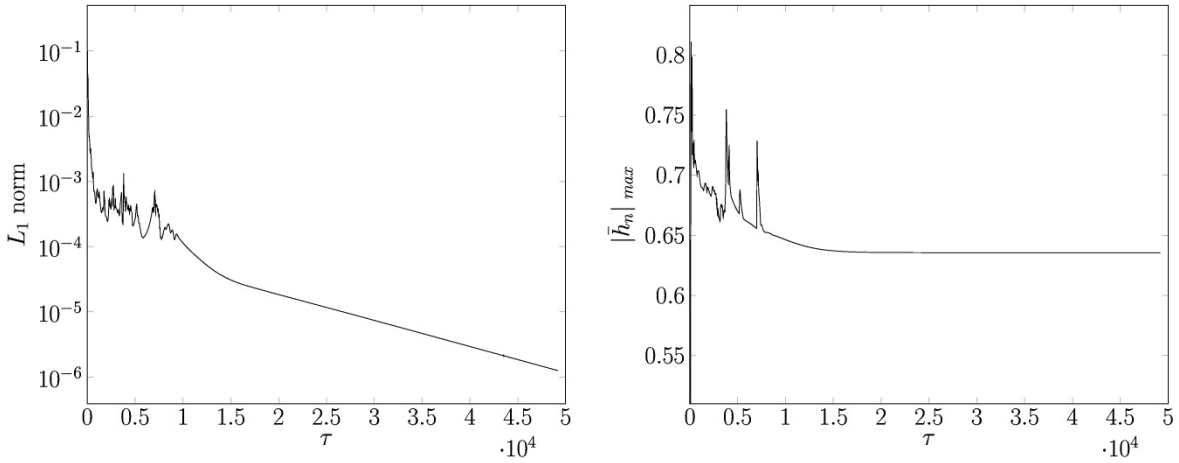

Figure 2. L_1 norm curve (left panel) and maximum height modulus (right panel) for a random initial pattern, $\Delta\tau$ = 0.1, ΔX = ΔY = 2, on a 256×256 nodes domain.

Figure 3 illustrates some major changes in the transient structure, from the initial to the steady state pattern formation. A hexagonal 2D weakly anisotropic structure grows rapidly from the random values; however, the defects take longer to be accommodated. From the L_1 norm and the maximum height modulus, it is expected that for $\tau = 20{,}000$ the hexagonal structure will be clear of defects, just as the pattern shown by $\tau = 49{,}200$. For each state, the Fast Fourier Transform (FFT) is also displayed for the central part of the domain, in order to observe the growing and arrangements of the modes which lead to the hexagonal pattern. It is important to emphasize that the final structure presents negative height values in the $\bar{h}^n$ function, with 0.65 being the valley. This result is physically coherent, since we expect the height to decay after the removal and rearrangement of surface atoms.

3.3 Initial Pattern: 1D Structure – Monomode $\vec{q} = q_o\vec{1}_x$

Another case of interest studied was for an initial pattern with sine function in the X direction, which represents a monomode 1D structure with wavevector $\vec{q} = q_o\vec{1}_x$. The pattern started with 14 wavelengths, being approximately half of the total number of wavelengths in the steady state from the previous case, which agrees with the critical wavelength calculated from the linear stability analysis and is placed inside the stable domain. From Figure 4 we follow a smooth pattern transition from the L_1 curve and a gently change of height values from the initial maximum modulus 0.1 (positive) up to 0.4 (negative). The wave amplitude goes initially from $(0;0.1)$ to $(-0.4;0)$ in the steady state, which is also consistent with the physical phenomenon of surface erosion.

In Figure 5 we can observe the growth of new harmonics and the decay of the initial, while maintaining the 1D structure and splitting the starting wavelength by two. The steady state is reached much more quickly when compared to the previous emergence of hexagons: while L_1 in the $q_o\vec{1}_x$ case takes approximately $2{,}000$ time steps of 0.1 to fall under $L_1 = 1 \times 10^{-6}$, it takes 250 times longer for the random initial condition. In terms of internal iterations, both pass on a maximum of six during the initial time steps and keep falling as they get closer to the steady state, when there are only two internal iterations for each time step.

4 CONCLUSION

In the present paper we have developed a finite-difference time splitting scheme for solving an anisotropic Kuramoto-Sivashinsky equation to describe a surface eroded by ion bombardment. The MMS was employed for code verification, and a second-order convergence was detected for coarser meshes comparison, while results between first and second-order convergence appeared for more refined meshes, suggesting a possible issue with the manufactured solution stability. Hexagonal patterns grew from a domain with random initial conditions, and for the monomode $\vec{q} = q_o\vec{1}_x$ case the wavelength split in two, meeting the critical wavenumber from the linear stability analysis. Both simulations were physically consistent with the sputtering phenomenon, reproducing ripple and hexagonal structure formation dynamics. Future work will investigate a greater variety of initial patterns and formalize the linear stability analysis for a better comparison with results.

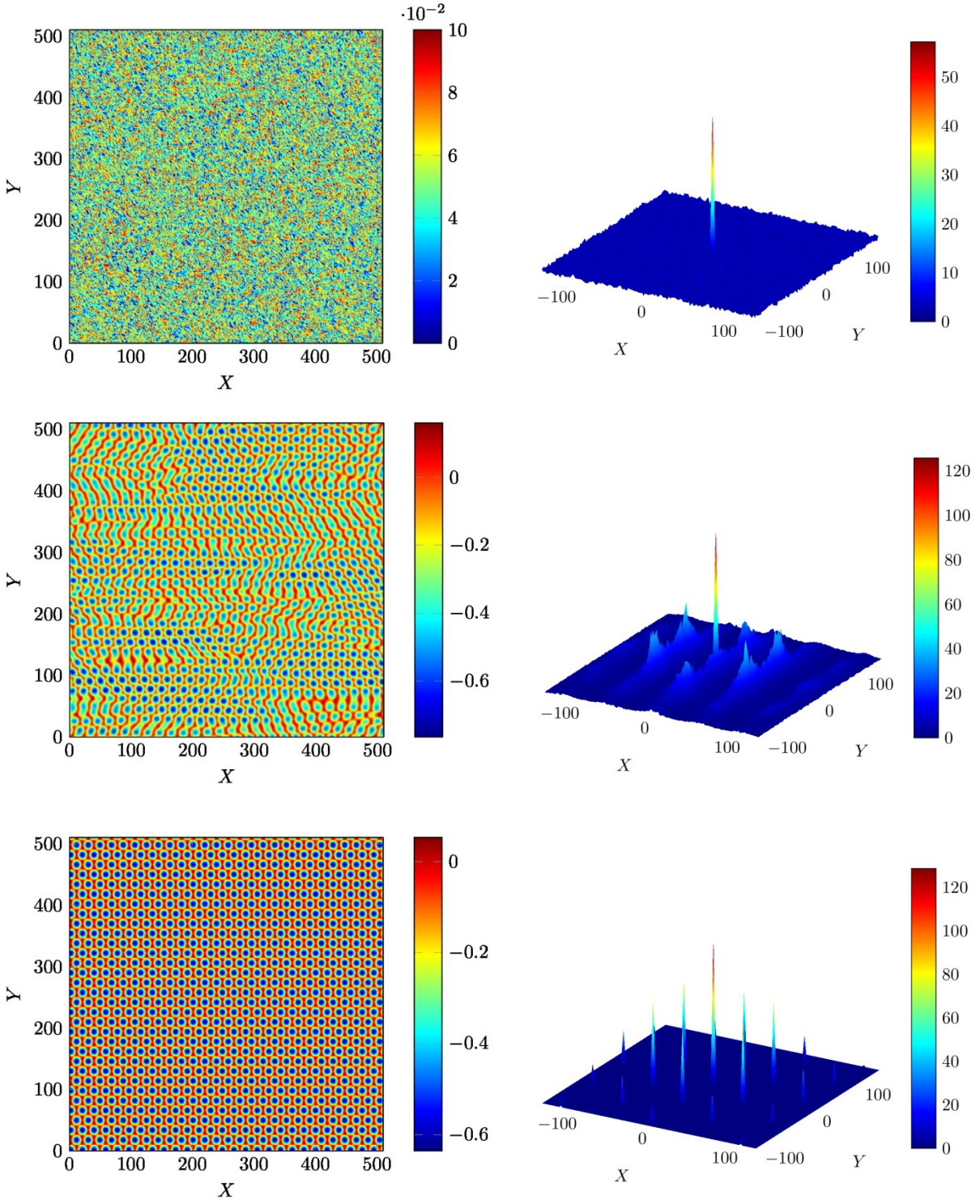

Figure 3. Surface height values $\bar{h}_n$ and their respective Fourier Transform for $\tau = 0$ (upper panel), $\tau = 200$ (middle panel) and $\tau = 49{,}200$ (bottom panel). A hexagonal pattern rises quickly from a random initial condition, while the defects are slowly eliminated, until the steady state is reached.

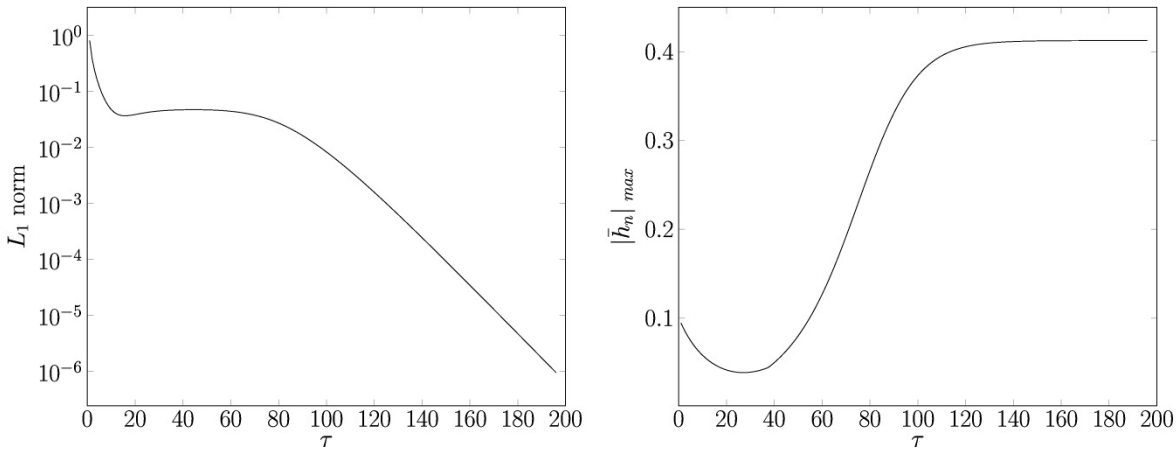

Figure 4. L1 norm curve (left panel) and maximum height modulus (right panel) for a monomode $q_o\vec{1}_x$ initial pattern, $\Delta\tau$ = 0.1, $\Delta X = \Delta Y$ = 2, on a 256×256 nodes domain.

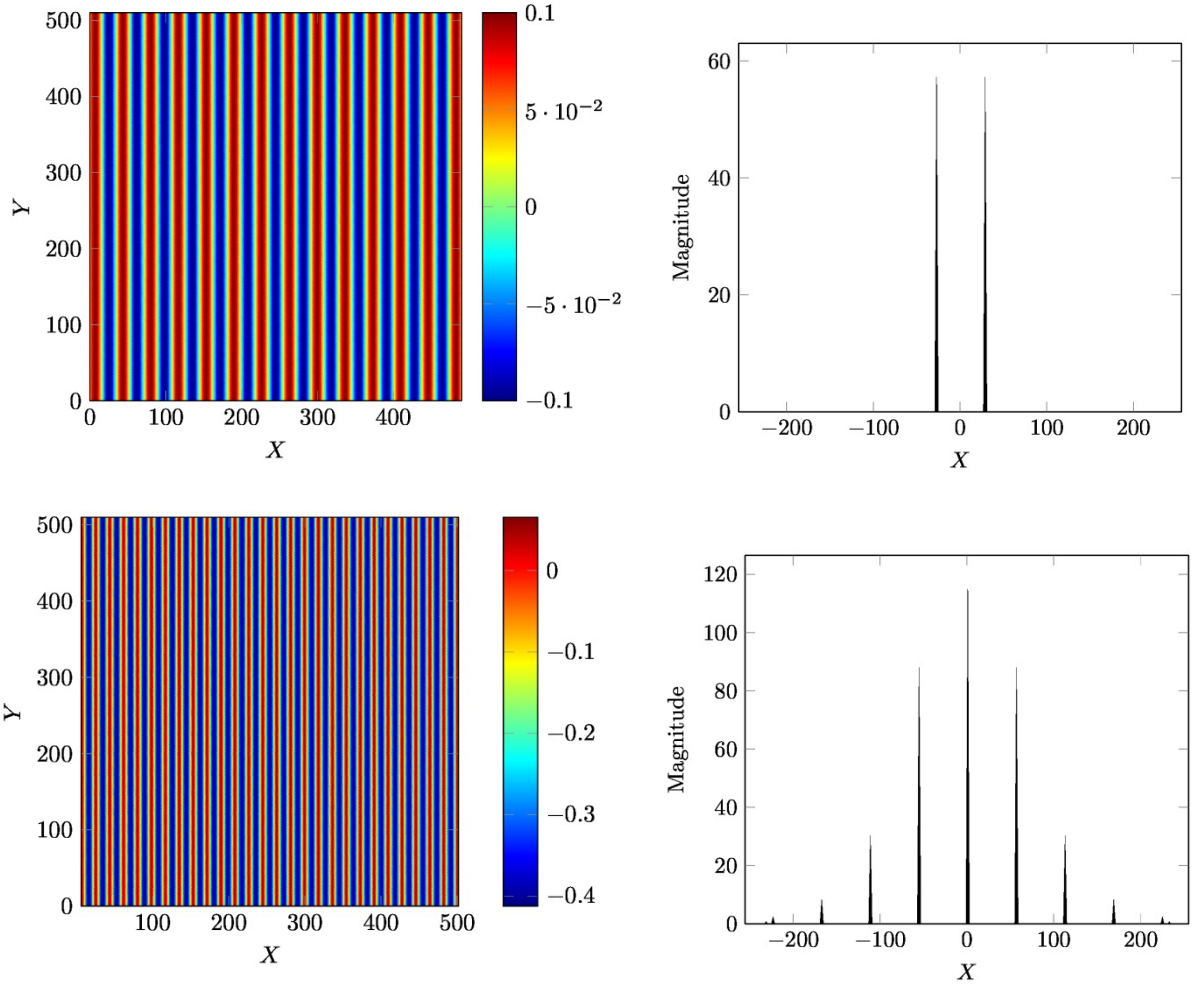

Figure 5. Surface height values $\bar{h}_n$ and their respective Fourier Transform for $\tau = 0$ (upper panel) and $\tau = 150$ (bottom panel). From a monomode $q_o\vec{1}_x$ initial pattern, the wavelengths are split in two with the decay and growth of new harmonics. The steady state maintains the 1D structure.

Acknowledgments

Eduardo Vitral acknowledges a fellowship from the Coordination for the Improvement of Higher Education-CAPES (Brazil). A FAPERJ Senior Researcher Fellowship is acknowledged by José Pontes.

REFERENCES

1 Chanson E, Chan WL. Spontaneous patterning of surfaces by low-energy ion beams. Topics in Applied Physics. 2010; 116: 53-71.
2 Ghoniem NM, Sehirlioglu A, Neff AL, Allain JP, Williams B, Sharghi-Moshtaghin R. Sputtering of molybdenum and tungsten nano rods & nodules irradiated with 150 eV argon ions. Applied Surface Science. 2015; 331: 299-308.
3 Mollick SA, Ghose D, Satpati B. Formation of Au-Ge nanodots by Au^- ion sputtering of Ge. Vacuum. 2014; 99: 289-293.
4 Wei Q, Zhou X, Joshi B, Chen Y, Li K-D, Wei Q, Sun K, Wang L. Self-assembly of ordered semiconductor nanoholes by ion beam sputtering. Advanced Materials. 2009; 21: 2865-2869.
5 Valbusa U, Boragno C, de Mongeot FB. Nanostructuring surfaces by ion sputtering. Journal of Physics: Condensed Matter. 2002; 14: 8153-8175.
6 Makeev MA, Cuerno R, Barabási A-L. Morphology of ion-sputtered surfaces. Nuclear Instruments and Methods in Physics B. 2002; 197: 185-227.
7 Rost M, Krug J. Anisotropic Kuramoto-Sivashinsky equation for surface growth and erosion. Physical Review Letters. 1995; 75: 3895-3897.
8 Christov CI, Pontes J, Walgraef D, Velarde MG. Implicit time splitting for fourth-order parabolic equations. Computing Methods in Applied Mechanics and Engineering. 1997; 148: 209-224.
9 Christov CI, Pontes J. Numerical scheme for Swift-Hohenberg Equation with strict implementation of Lyapunov Functional. Mathematical and Computer Modelling. 2002; 35: 87-99.
10 Sigmund P. Theory of sputtering I Sputtering yield of amorphous and polycrystalline targets. Physical Review. 1969; 184: 383-416.
11 Bradley RM, Harper JM. Theory of ripple topography induced by ion bombardment. Journal of Vacuum Science & Technology A. 1988; 6: 2390-2395.
12 Cuerno R, Barabási A-L. Dynamic scaling of ion-sputtered surfaces. Physical Review Letters. 1995; 74: 4746-4749.
13 Keller A, Facsko S. Ion-induced nanoscale ripple patterns on Si surfaces: theory and experiment. Materials. 2010; 3: 4811-4841.
14 Douglas J, Rachford HH. On the numerical solution of the heat conduction problems in two and three space variables. Transactions of the American Mathematical Society. 1956; 82: 421-439.
15 Yanenko NN. The Method of Fractional Steps. New York: Springer; 1971.
16 Malaya N, Estacio-Hiroms KC, Stogner RH, Schulz KW, Bauman PT, Carey GF. MASA: a library for verification using manufactured and analytical solutions. Engineering with Computers. 2013; 29: 487-496.
17 Roache PJ. Code verification by the method of manufactured solutions. Journal of Fluids Engineering. 2002; 124: 4-10.